Science AAAS

Supplementary Materials for

Pair wave function symmetry in UTe_2 from zero-energy surface state visualization

Qiangqiang Gu *et al*.

Corresponding authors: Qiangqiang Gu, qiangqianggu2016@gmail.com; J. C. Séamus Davis, jcseamusdavis@gmail.com; Dung-Hai Lee, dunghai@berkeley.edu

Science **388**, 938 (2025)
DOI: 10.1126/science.adk7219

The PDF file includes:

Materials and Methods
Supplementary Text
Figs. S1 to S8
Tables S1 and S2
References

Materials and Methods

Our measurements on UTe_2 crystals were carried out in a custom-built scanned Josephson/Andreev tunneling microscope. The UTe_2 samples were grown by the chemical vapor transport (CVT) method as in Ref. 11 and exhibit a $T_c \approx 1.6$ K. The (0-11) surface of the sample was cleaved in cryogenic ultrahigh vacuum at a temperature of ~4.2 K. The sample was then immediately transferred into the STM head. Measurements were carried out using Nb tips at base temperatures of ~4.2 K and ~280 mK. The superconducting Nb tips were prepared by field emission.

Supplementary Text

1. Topological surface bands of nodal spin-triplet superconductors

Three-dimensional (3D) nodal, odd parity superconductors are analogous to the 3D Weyl semimetal state. As shown in Main Text Fig. 1A, for real-space surfaces parallel to the nodal $\hat{x}$ -axis the in-plane momenta are good quantum numbers. The momentum axis passing perpendicular through the nodes separate the two-dimensional (2D) reciprocal spaces spanned by the in-plane momentum into topologically distinct regions. This is manifested by the presence or absence of topological surface bands (TSBs). In general, the boundary between these topologically inequivalent regions marks the topological phase transition, where the superconducting gap closes.

The 2D Brillouin zone of a crystal surface parallel to the $\Delta_{\boldsymbol{k}}$ nodal axis, namely, the *a*-*b* plane, shows a line of zero-energy TSB states dubbed a Fermi arc, which connects the two points representing the projections of the 3D $\Delta_{\boldsymbol{k}}$ nodal wavevectors $\pm k_n$ onto this 2D zone. Moreover, the TSB of nodal odd parity superconductors on the surface of *a*-*b* plane is represented by a 2D band dispersion for $E_{\mathrm{TSB}}(k_x, k_y)$ within the radius of the Fermi surface in the k_z = 0 plane (Main Text Fig. 1B). An approximate density-of-states of TSB quasiparticle states can be calculated using

$$N(E) = \sum_{k_{x,y}} \frac{\Gamma/\pi}{\left(E - E_{TSB}(k_x, k_y)\right)^2 + \Gamma^2} \qquad \text{(S.1)}$$

where Γ is a momentum independent quasiparticle broadening parameter (5 μeV is used here). At the surface, when integrated over (k_x, k_y) in the 2D Brillouin zone, the flat Fermi arc at E = 0 contributes strongly to a sharp zero-energy peak surface density of states $N(E)$ (Main Text Fig. 1C).

2. Candidate superconductive order parameters for UTe_2 with D_{2h} symmetry

The crystal symmetry point-group for UTe_2 is D_{2h} with space group *Immm* which, if we consider spin-orbit coupling, features four possible, odd-parity order-parameter symmetries: A_u, B_{1u}, B_{2u}, and B_{3u} (Table S1). All single-component representations below preserve time-reversal symmetry and three have zeros (nodes) in Δ_k whose axial alignment is outlined in Table S1.

OP	$\boldsymbol{d}$	Δ_k	Nodal Axis
A_u	$\alpha k_x\hat{\boldsymbol{x}}$ $\beta k_y\hat{\boldsymbol{y}}$ $\gamma k_z\hat{\boldsymbol{z}}$	$(-k_x + ik_y)\|\uparrow\uparrow\rangle$ $+(k_x + ik_y)\|\downarrow\downarrow\rangle$ $+k_z(\|\uparrow\downarrow\rangle + \|\downarrow\uparrow\rangle)$ If $\alpha = \beta = \gamma = 1$	None
B_{1u}	$\alpha k_y\hat{\boldsymbol{x}}$ $\beta k_x\hat{\boldsymbol{y}}$ $\gamma k_x k_y k_z\hat{\boldsymbol{z}}$	$(-k_y + ik_x)\|\uparrow\uparrow\rangle$ $+(k_y + ik_x)\|\downarrow\downarrow\rangle$ If $\alpha = \beta = 1, \gamma = 0$	*c*
B_{2u}	$\alpha k_z\hat{\boldsymbol{x}}$ $\beta k_x k_y k_z\hat{\boldsymbol{y}}$ $\gamma k_x\hat{\boldsymbol{z}}$	$k_z(\|\downarrow\downarrow\rangle - \|\uparrow\uparrow\rangle)$ $+k_x(\|\uparrow\downarrow\rangle + \|\downarrow\uparrow\rangle)$ If $\alpha = \gamma = 1, \beta = 0$	*b*
B_{3u}	$\alpha k_x k_y k_z\hat{\boldsymbol{x}}$ $\beta k_z\hat{\boldsymbol{y}}$ $\gamma k_y\hat{\boldsymbol{z}}$	$ik_z(\|\uparrow\uparrow\rangle + \|\downarrow\downarrow\rangle)$ $+k_y(\|\uparrow\downarrow\rangle + \|\downarrow\uparrow\rangle)$ If $\alpha = 0, \beta = \gamma = 1$	*a*

Table S1. Single-component odd-parity spin-triplet superconductive order parameters for D_{2h} symmetry, considering the spin-orbit coupling.

Linear combinations of these D_{2h} order-parameters are also possible which break time-reversal symmetries, resulting in chiral states, shown in Table S2. Two have nodes aligned with the crystal ***c***-axis, and two aligned with the ***a***-axis. A time-reversal symmetry breaking chiral order parameter breaks down symmetries of the lattice, while remaining an irreducible representation (IR) of the D_{2h} point symmetry group.

OP	$\boldsymbol{d}$	Δ_k	Nodal Axis
A_u+iB_{1u}	$(\alpha_1 k_x + i\alpha_2 k_y)\hat{\boldsymbol{x}}$ $(\beta_1 k_y + i\beta_2 k_x)\hat{\boldsymbol{y}}$ $(\gamma_1 k_z + i\gamma_2 k_x k_y k_z)\hat{\boldsymbol{z}}$	$-2k_x\|\uparrow\uparrow\rangle$ $+i2k_y\|\downarrow\downarrow\rangle$ If $\alpha_{1,2} = \beta_{1,2} = 1\ \gamma_{1,2} = 0$	*c*
B_{2u}+iB_{3u}	$(\alpha_1 k_z + i\alpha_2 k_x k_y k_z)\ \hat{\boldsymbol{x}}$ $(\beta_1 k_x k_y k_z + i\beta_2 k_z)\hat{\boldsymbol{y}}$ $(\gamma_1 k_x + \gamma_2 i k_y)\hat{\boldsymbol{z}}$	$(k_x + ik_y)(\|\uparrow\downarrow\rangle + \|\downarrow\uparrow\rangle)$ If $\alpha_{1,2} = \beta_{1,2} = 0\ \gamma_{1,2} = 1$	*c*
A_u+iB_{3u}	$(\alpha_1 k_x + i\alpha_2 k_x k_y k_z)\hat{\boldsymbol{x}}$ $(\beta_1 k_y + i\beta_2 k_z)\hat{\boldsymbol{y}}$ $(\gamma_1 k_z + i\gamma_2 k_y)\hat{\boldsymbol{z}}$	$(ik_y - k_z)(\|\uparrow\uparrow\rangle + \|\downarrow\downarrow\rangle) +$ $(k_z + ik_y)(\|\uparrow\downarrow\rangle + \|\downarrow\uparrow\rangle)$ If $\alpha_{1,2} = 0, \beta_{1,2} = \gamma_{1,2} = 1$	*a*
B_{1u}+iB_{2u}	$(\alpha_1 k_y + i\alpha_2 k_z)\ \hat{\boldsymbol{x}}$ $(\beta_1 k_x + i\beta_2 k_x k_y k_z)\hat{\boldsymbol{y}}$ $(\gamma_1 k_x k_y k_z + \gamma_2 k_x)\hat{\boldsymbol{z}}$	$(k_y + ik_z)(-\|\uparrow\uparrow\rangle + \|\downarrow\downarrow\rangle)$ If $\alpha_{1,2} = 1, \beta_{1,2} = \gamma_{1,2} = 0$	*a*

Table S2. Linear combinations of D_{2h} order-parameters give rise to chiral spin-triplet superconductive order parameters with ***a***-axis and ***c***-axis nodes.

Finally, given the number of free parameters in Tables S1 and S2 there are, of course, an enormous number of other possibilities. For example in the B_{3u} state with $\boldsymbol{d} = (0, \beta k_z, \gamma k_y)$, by choosing real β imaginary γ, their relative phase could (instead of being set at 0 as we do throughout) be chosen as $\pi/2$. Another somewhat equivalent example would be a choice of real α imaginary β for the A_u state. However, in these and equivalent cases one is enforcing the breaking of time-reversal symmetry so that the consequent order parameters are not IR of the D_{2h} symmetry group. Furthermore, an admixture of two single components that is non-chiral is allowable but may break further symmetries of the lattice, such as mirror and rotational symmetries. While such order parameters could obviously exist in nature, they are not the subject of our studies nor those of any other UTe_2 researchers that we are aware of.

3. Experimental evidence of superconductive order parameters

Identifying the $\Delta_{\boldsymbol{k}}$ symmetry of UTe_2 with a specific IR of D_{2h} or with some linear combinations thereof in macroscopic experiments is complicated, and the status of UTe_2 $\Delta_{\boldsymbol{k}}$ remains indeterminate. For example, a magnetic susceptibility upon entering the superconducting phase that is equivalent to Pauli paramagnetism, is deduced from minimal suppressions of the Knight shift (*14,15,17*) and used to adduce spin-triplet pairing (because spin-1 eigenstates typically retain their magnetic moments). Some NMR studies measuring this change of the spin susceptibility across T_c report a decrease in the Knight shift in all directions and hypothesize the isotropically gapped A_u state (*17*), while other NMR studies detect a reduction in the Knight shift along the $\boldsymbol{b}$ and $\boldsymbol{c}$ axes only, thence hypothesizing B_{3u} pairing symmetry (*18*). Magnetic field orientation of the thermal conductivity (CVT) indicates a superconducting energy gap with point nodes parallel to the crystal $\boldsymbol{a}$-axis (*19*), while other field-oriented thermal conductivity (MFM) measurements (*20*) report isotropic results and hypothesize an A_u order parameter symmetry. Field-oriented specific heat measurements reveal peaks around the crystal $\boldsymbol{a}$-axis implying point nodes oriented along this direction and hypothesize an order parameter with chiral $A_u + iB_{3u}$ or helical B_{3u} symmetries (*21*). Some electronic specific heat studies (CVT) report two specific heat peaks and hypothesize a chiral $A_u + iB_{1u}$ or $B_{2u} + iB_{3u}$ order parameter (*22*), while other specific heat studies (MFM) detect only a single specific heat peak and thus hypothesize a single component order parameter (*23*). London penetration depth measurements of superfluid density report anisotropic saturation consistent with nodes along the $\boldsymbol{a}$-axis suggesting B_{3u} symmetry pairing for a cylindrical Fermi surface (*24*), while other penetration depth measurements exhibiting an $n \leq 2$ power law dependence of the penetration depth on temperature motivate a hypothesis of $B_{3u} + iA_u$ pairing symmetry (*25*). Scanning tunneling microscopy experiments (CVT) in the (0-11) plane parallel to $\boldsymbol{a}$-axis show energy-reversed particle-hole symmetry breaking at opposite mirror-symmetric UTe_2 step edges (*26*) with the consequent hypothesis of a chiral surface state $B_{1u} + iB_{2u}$ whose nodes are aligned to the $\boldsymbol{a}$-axis. Polar Kerr effect measurements (CVT) report a field-induced Kerr rotation indicating the presence of time-reversal symmetry breaking and hypothesize chiral $B_{2u} + iB_{3u}$ or $A_u + iB_{1u}$ pairing (*22*) with nodes aligned to the $\boldsymbol{c}$-axis, while other polar Kerr effect measurements (MFM) report no detectable spontaneous Kerr rotation (*27*).

4. SIP model

We model a planar interface between an *s*-wave and a nodal *p*-wave superconductor (SIP), in which is located a topological surface band. Firstly, we construct the general four component Bogoliubov-de Gennes (BdG) Hamiltonian for a superconductor,

$$H = \sum_{k} \psi^{+}(\boldsymbol{k}) H(\boldsymbol{k}) \psi(\boldsymbol{k}),\ \psi(\boldsymbol{k}) = (c_{\boldsymbol{k}\uparrow}, c_{\boldsymbol{k}\downarrow}, c_{-\boldsymbol{k}\uparrow}^{+}, c_{-\boldsymbol{k}\downarrow}^{+})^{\mathrm{T}} \tag{S.2}$$

H_{Nb} is the Hamiltonian of an *s*-wave superconductor Nb with

$$H_{\mathrm{Nb}}(\boldsymbol{k}) = \begin{pmatrix} \epsilon_{\mathrm{Nb}}(\boldsymbol{k})\sigma_0 & \Delta_{\mathrm{Nb}}(i\sigma_2) \\ \Delta_{\mathrm{Nb}}^{*}(-i\sigma_2) & -\epsilon_{\mathrm{Nb}}(-\boldsymbol{k})\sigma_0 \end{pmatrix} \tag{S.3}$$

Here $\epsilon_{\mathrm{Nb}}(\boldsymbol{k})$ is the band structure of Nb, Δ_{Nb} is the Nb superconducting order parameter (in the computation we take Δ_{Nb} to be momentum independent), and $\sigma_{0,1,2,3}$ are the four components of Pauli matrices. $H_{\mathrm{UTe_2}}$ is the Hamiltonian of the putative *p*-wave superconductor with

$$H_{\mathrm{UTe_2}}(\boldsymbol{k}) = \begin{pmatrix} \epsilon_{\mathrm{UTe_2}}(\boldsymbol{k})\sigma_0 & \Delta_{\mathrm{UTe_2}}(\boldsymbol{k}) \\ \Delta_{\mathrm{UTe_2}}^{+}(\boldsymbol{k}) & -\epsilon_{\mathrm{UTe_2}}(-\boldsymbol{k})\sigma_0 \end{pmatrix} \tag{S.4}$$

Here $\epsilon_{\mathrm{UTe_2}}(\boldsymbol{k})$ is the band structure containing a model spherical Fermi surface of UTe_2, and $\Delta_{\mathrm{UTe_2}}(\boldsymbol{k})$ is a 2×2 odd parity pairing matrix given by $\Delta_{\mathrm{UTe_2}}(\boldsymbol{k}) \equiv \Delta_{\mathrm{UTe_2}} i(\boldsymbol{d} \cdot \boldsymbol{\sigma})\sigma_2$. Both $\epsilon_{\mathrm{UT}e_2}(\boldsymbol{k})$ and $\epsilon_{\mathrm{Nb}}(\boldsymbol{k})$ are nearest neighbor tight binding dispersions on a simple cubic lattice with the same lattice constant and are modeled as $\cos(k_x) + \cos(k_y) + \cos(k_z) - 2$ in the unit of meV. Given the focus of this project on the interplay of pairing symmetry, the exact band structures for Nb and UTe_2 are irrelevant.

We compare two candidate order parameters for UTe_2, one built from the IR B_{3u} of Table S1. This is the non-chiral gap function with nodes in the $\boldsymbol{a}$ direction. The second order parameter considered is the chiral state $A_u + iB_{3u}$ with nodes also in the $\boldsymbol{a}$ direction (for $B_{1u} + iB_{2u}$ pairing the conclusions are the same). Below we present the 2×2 pairing matrix in momentum space derived using $\Delta_k \propto i[\boldsymbol{d}(\boldsymbol{k}) \cdot \boldsymbol{\sigma}]\sigma_2$.

For B_{3u}: $\boldsymbol{d} = (0, k_z, k_y)$

$$\Delta_{\boldsymbol{k}} \propto \begin{pmatrix} ik_z & k_y \\ k_y & ik_z \end{pmatrix} \tag{S.5}$$

For $A_u + iB_{3u}$: $\boldsymbol{d} = (0, k_y + ik_z, k_z + ik_y)$

$$\Delta_{\boldsymbol{k}} \propto \begin{pmatrix} -k_z + ik_y & k_z + ik_y \\ k_z + ik_y & -k_z + ik_y \end{pmatrix} \tag{S.6}$$

Lastly, we model the tunneling Hamiltonian between the Nb and UTe_2 interfaces as

$$H_T = -|M| \sum_{\boldsymbol{k}_\parallel} [\psi^\dagger_{\mathrm{Nb},\boldsymbol{k}_\parallel} \sigma_3 \otimes \sigma_0 \, \psi_{\mathrm{UTe_2},\boldsymbol{k}_\parallel} + h.c.] \tag{S.7}$$

where $\boldsymbol{k}_\parallel = (k_x, k_y, 0)$ is the quasiparticle momentum parallel to the interface. The model developed consists of twenty Nb layers adjacent to fifty UTe_2 layers stacked in the $\hat{\boldsymbol{c}}$ direction, with tunneling between the surface layer of each superconductor (Fig. S1A). We then derive the eigenvalues and eigenvectors of the total Hamiltonian $H = H_{\mathrm{Nb}} + H_{\mathrm{UTe_2}} + H_{\mathrm{T}}$. We keep those eigenenergies whose wavefunction weight exceeds a certain lower bound (10^{-3} weight on the top surfaces of Nb and UTe_2) and plot the eigenvalues of the Hamiltonian against k_y with k_x as a parameter. For all calculations we set the superconducting gap magnitude of UTe_2 to be 0.25 meV to approximate the gap magnitude of the sample, and set the Nb gap to 1.25 meV to approximate the gap of the STM tip.

At $k_x = 0$, when the tunneling matrix $M = 0$, the band dispersion on Nb top layer shows a continuum within the full Nb gap energy (Fig. S1B). Fig. S1C shows the band dispersion on UTe_2 top layer, TSBs are formed on the UTe_2 surface indicated by red lines and the extra bulk bands are indicated by blue lines. The observables are dominated by the topological surface band consisting of one sheet for the $A_u + iB_{3u}$ model or two sheets for B_{3u} alone.

To highlight TSB states, Figures 2B,C of the main text show the band dispersion on the top surface of UTe_2 at $k_x = 0$ for chiral $A_u + iB_{3u}$ and non-chiral B_{3u} state when M is set to zero, without the effect of Nb. We have checked that the nature of the spectrum remains independent of the bound so long as the number of layers is sufficiently large.

For a chiral superconducting order parameter with symmetry $A_u + iB_{3u}$, the TSB has a two-fold degenerate chiral TSB starting from negative $\Delta_{\mathrm{UTe_2}}$, positive k_y to positive $\Delta_{\mathrm{UTe_2}}$, negative k_y (Main Text Fig. 2B). This is the expected chiral surface state dispersion in which the TSB quasiparticles break time-reversal symmetry. In comparison, the non-chiral order parameter with symmetry B_{3u} develops two TSB branches, which are symmetric with respect to the $k_y = 0$ axis and thus do not break time-reversal symmetry (Main Text Fig. 2C). The spectra for both chiral and non-chiral order parameters feature TSBs for $-0.5\pi < k_x < 0.5\pi$ where $(\pm 0.5\pi, 0, 0)$ are the locations of the gap nodes. For $|k_x| > 0.5\pi$ there are no in-gap states and at $k_x = \pm 0.5\pi$ the gap closes. Figures S1E,F show the 3D representation of these two chiral and non-chiral TSB.

To investigate the tunneling effect between Nb and UTe_2, we calculate the band dispersion on Nb top surface in Fig. S1D when $|M|$ is nonzero (0.2 meV is used in the calculation). The tunneling process can be categorized into two types based on the energy range. Outside the Nb gap Δ_{Nb}, the UTe_2 bulk states are overlapped with Nb states via single-particle tunneling. Inside Δ_{Nb}, the bulk states of UTe_2 states cannot penetrate into the bulk of Nb and contribute to the tunneling conductance. However, and most importantly, we find that the TSBs of UTe_2 can tunnel into the bulk of Nb in the form of Cooper pairs by the Andreev reflection process without the energy cost of the Nb gap. (Fig. S1D).

5. Hybridization of a *p*-wave TSB with an *s*-wave electrode

To investigate the effect of tunneling between a Nb tip and UTe_2 we set a finite tunneling amplitude $|M| > 0$ and plot the $k_x = 0$ BdG spectrum derived from the three-term Hamiltonian $H = H_{\mathrm{Nb}} + H_{\mathrm{UTe_2}} + H_{\mathrm{T}}$. In Main Text Figs. 3A and B we demonstrate the effect of increasing the magnitude of $|M|$ (which corresponds to decreasing the tunnel junction resistance experimentally). When $|M|$ increases in the SIP model for a chiral $A_u + iB_{3u}$ superconductor, the surface state develops two branches at different momenta while maintaining zero-energy crossings (Main Text Fig. 3A). Thus, the Andreev conductance peak in $dI/dV|_{\mathrm{SIP}}$ remains as a single maximum at zero-energy with reducing STM junction resistance. As $|M|$ increases in the SIP model for a non-chiral B_{3u} superconductor, the TSB splits into two particle-hole symmetric energy bands with symmetric momentum dependence with respect to the $k_y = 0$ axis. Thus, the zero-energy Andreev conductance peak in $dI/dV|_{\mathrm{SIP}}$ must split into two finite energy $dI/dV|_{\mathrm{SIP}}$ maxima which further move apart in energy as the junction resistance is reduced. From the $N(E)$ calculation of the TSB as implemented in Eqn. S1, we find that with increasing $|M|$, the single maximum at zero-energy in $N(E)$ remains unchanged for chiral $A_u + iB_{3u}$ state while it splits into two peaks for non-chiral B_{3u} state.

The key to understanding the TSB splitting is the relative phase $\delta\phi$ between the Nb and UTe_2 order parameters at the interface. When $|M| = 0$, the gapless edge states of the B_{3u} pairing superconductor are protected by time-reversal symmetry ($T^2 = -I$ and Z_2 classification). When $|M| > 0$ for the B_{3u} state the relative phase $\delta\phi$ evolves to $\frac{\pi}{2}$ (Fig. S2B) lowering the total electronic energy of the system by reducing the energies of all occupied TSB states $E < 0$. When $\delta\phi = \frac{\pi}{2}$ the time-reversal symmetry within the SIP junction is broken because upon the time-reversal $e^{i\delta\phi} = i \rightarrow e^{-i\delta\phi} = -i$. Thus, if UTe_2 is an odd-parity superconductor with non-chiral B_{3u} state whose isolated Δ_k preserves time-reversal symmetry, the SIP relative phase becomes $\delta\phi = \frac{\pi}{2}$ due to proximity of the *s*-wave electrode. Under such condition the gapless TSB is no longer protected. Conversely, if UTe_2 is a chiral superconductor with an order parameter such as $A_u + iB_{3u}$ then TRS is broken without the influence of the *s*-wave superconducting STM tip. In that case the topological classification is Z, and the gapless TSB does not require any symmetry to remain protected and so remains gapless regardless of $|M|$ (Fig. S2A).

6. The effect of mirror symmetry breaking by the STM tip

Another potential cause of the TSB splitting phenomenology is possible if the gap function of UTe_2 exhibits B_{3u} pairing. In that case the gap function is independent of k_x. Consequently, the BdG Hamiltonian is invariant under an anti-unitary symmetry (T_1): $\hat{T}_1^{-1}\Psi_{k_x,k_y,k_z}T_1 = iI\sigma_y\Psi_{k_x,-k_y,-k_z}$. Furthermore, since the SIP model assumes planar tunneling, where translational symmetry parallel to the surface is preserved, an additional mirror symmetry (M_r) exists: $M_r^{-1}\Psi_{k_x,k_y,k_z}M_r = \Psi_{-k_x,k_y,k_z}$. Together, $M_r \cdot T_1$ restores time-reversal symmetry. In an STM setup involving point tunneling, the mirror symmetry (M_r) can be broken, which compromises time-reversal symmetry. This symmetry breaking allows a gap to open in the non-chiral TSB. In general, this effect also becomes more pronounced as the tip-sample conductance increases.

7. Andreev conductance of *s*-wave electrode through a *p*-wave TSB

A key consideration is the effect of hybridization of a *p*-wave TSB with an *s*-wave electrode on the Andreev conductance across the junction between the *p*-wave and *s*-wave superconductors. The origin of Andreev reflection for superconductors is the anomalous term $\sum_{\boldsymbol{k}}\sum_{\alpha,\beta}[\,\Delta_{\alpha\beta}(\boldsymbol{k})c^+_{\alpha,\boldsymbol{k}}\,c^+_{\beta,-\boldsymbol{k}} + h.c.]$ (here α and β label the spin of the electron) in the

Hamiltonian. This term allows an incident electron (hole) impacting on an order parameter $\Delta_{\alpha,\beta}(\boldsymbol{k})$ to reflect as a hole (electron) as depicted in Main Text Fig. 2A.

Most simply, a single Andreev reflection transfers two electrons (holes) between the tip and the sample (Main Text Fig. 2D). Based on the S-matrix approach, the formula to compute the Andreev conductance of the SIP Model is

$$a(V) = \frac{8\pi^2 t_{\text{eff}}^4 e^2}{h} \sum_n \frac{\langle\phi_n|P_h|\phi_n\rangle\langle\phi_n|P_e|\phi_n\rangle}{(eV - E_n)^2 + \pi^2 t_{\text{eff}}^4[\langle\phi_n|P_h|\phi_n\rangle + \langle\phi_n|P_e|\phi_n\rangle]^2} \quad \text{(S.8)}$$

Here $|\phi_n\rangle$ is the projection of the n^{th} TSB eigenfunction onto the top UTe_2 surface, and P_e and P_h are the electron and hole projection operators acting on the UTe_2 surface and V is the bias voltage. Note that the Andreev conductance $a(V)$ is different from $N(E)$ in Eqn. S1. However, both equations count the related eigenvalues through the integral over the whole TSB.

Thus, in principle, the sharp zero-energy peak of the calculated $N(E)$ in Main Text Fig. 1C will be clearly reflected in the sharp zero-energy peak of Andreev conductance $a(V)$. Figure S3A shows the schematic of the TSB generated Andreev reflection to the *s*-wave electrode. Specifically within the SIP model, we plot in Fig. S3B the calculated $a(V)$ from Eqn. S8 which predicts a sharp peak in Andreev conductance surrounding zero-bias. In this figure we have divided the total Andreev conductance by the number of transverse $k_{\parallel}$ channels to mimic the point tunneling of STM.

8. Topological surface band and Andreev phenomenology at UTe_2 (0-11) surface

A typical topograph of the UTe_2 crystal cleave surface (0 -1 1) is presented in Fig. S4A and its Fourier transform is shown in Fig. S4B. To demonstrate empirically that the zero-energy state detected in $dI/dV|_{\text{SIP}}$ is a result specifically of the UTe_2 TSB we present a linecut across a cluster of impurity atoms in Fig. S5. This cluster is likely made up of Nb atoms which have been accidentally transferred from the Nb STM tip to the surface of the sample. The sub-gap conductance quickly collapses to zero and the $dI/dV|_{\text{SIP}}$ spectra become fully gapped as the tip measures across the metallic cluster (Fig. S5). The zero-energy $dI/dV|_{\text{SIP}}$ peak on the unperturbed surfaces is therefore not an artefact of the Nb scanning tip, but an omnipresent feature of the UTe_2 (0 -1 1) surface.

Here it is important to emphasize the zero bias peak cannot be attributed to the Josephson current. This can be demonstrated clearly by plotting typical measured Andreev zero-bias conductance $a(0)$, as shown in Fig. S6A, versus tip-sample junction resistance R on the same plot with the maximum possible zero-bias conductance which could be generated by the Josephson effect $g(0)$, here exemplified by measured Nb/$NbSe_2$ Josephson zero-bias conductance data. These results are presented in Fig. S6B. At high R, the intensity of measured $a(0)$ of Nb/UTe_2 is many orders of magnitude larger than it could possibly be due to Josephson currents. Moreover measured $a(0)$ for Nb/UTe_2 first grows linearly in decreasing R but then diminishes steeply as R is reduced further, whereas the zero-bias conductance due to Josephson currents $g(0)$ grows rapidly as $1/R^2$ as exemplified in the Nb/$NbSe_2$ $g(0)$ data. Most importantly one does not expect the zero-bias peak due to the Josephson effect to split when R is low. These highly repeatable and internally consistent experimental facts demonstrate the absence of detectable Josephson currents between Nb electrodes and the UTe_2 (0-11) termination surface.

9. Phase fluctuation effect on tip-induced time-reversal symmetry breaking

These data and SIP model raise the issue of fluctuations in the relative phase $\delta\phi$ between the Nb and UTe_2 order parameters when interacting predominantly by Andreev coupling. Recall that if UTe_2 is an odd-parity superconductor with a nodal, non-chiral, time-reversal conserving state Δ_k , the minimum energy SIP relative phase is $\delta\phi = \frac{\pi}{2}$ due to proximity of the *s*-wave electrode. This effect will spit the zero-bias Andreev conductance as shown in Fig. S6A. To evaluate if thermal fluctuations in $\delta\phi$ should wipe out the peak splitting effect for the realistic parameterization of Δ_k of UTe_2, temperature T and junction resistance R, we calculate the TSB density-of-states $N(E)$ when $\delta\phi = \frac{\pi}{2}$ and when $N(E)$ is averaged over the whole range $0 < \delta\phi < \pi$. The result as presented in Fig. S7 demonstrates that realistic phase fluctuations will not wipe out *s*-wave tip-induced $N(E)$ splitting, thus preserving the Andreev $a(V)$ conductance splitting.

10. Imaging and Fourier analysis of $dI/dV|_{\mathrm{SIP}}$: Andreev conductance modulation $\boldsymbol{S}_3$

Imaging Andreev conductance reveals spatial modulations in the zero-energy $dI/dV|_{\mathrm{SIP}}$ (Fig. S8). These data are measured at a junction resistance of 5 MΩ in the same field of view as the topograph in Fig. S8A. Fourier transformation of this $a(\boldsymbol{r}, 0)$ Andreev conductance map, $a(\boldsymbol{q}, 0)$, shows new features that only exist in the superconducting state. Among them is the new wavevector $\boldsymbol{S}_3$ (Fig. S8) whose identification requires the following considerations.

First, if $\boldsymbol{S}_3$ is a normal-state CDW, it must appear above T_C. But in all our experimental studies $\boldsymbol{S}_3$ is only observed in the superconducting phase (Main Text Fig. 4G). Moreover, a CDW is highly unlikely to exist only in the very narrow energy range of ~ ±150 μeV (Fig. S8D) where $\boldsymbol{S}_3$ is observed. Thus, $\boldsymbol{S}_3$ cannot be considered a normal-state CDW.

Second, interaction between uniform superconductivity of UTe_2 with a pre-existing CDW (*35*) or PDW (*34*) both occurring with the same wavevector $\boldsymbol{Q}$, cannot induce a CDW or a PDW at $\boldsymbol{Q}/2$ as this is ruled out by Ginzburg-Landau theory (*48*).

Third, in the SIP model the projected gap nodes on the surface BZ are not isolated $\boldsymbol{k}$ points since they are connected by a zero energy Fermi arc leading to finite DOS. Thus, the narrow energy distribution of $\boldsymbol{S}_3$ is more consistent with QPI pertinent to the gap nodes along the k_x direction, because quasiparticle scattering between the projected gap nodes and/or the Fermi arc connecting the two gap nodes naturally occur at $E = 0$, and it will be quickly diminished when the energy moves away from zero.

Based on the above experimental arguments, the new wavevector $\boldsymbol{S}_3$ we detect cannot represent a preexisting CDW nor a superconductivity induced CDW or PDW. However, it could represent quasiparticle scattering resulting from two superconducting gap nodes along the $\hat{\boldsymbol{a}}$ direction.

11. Spherical Fermi surface of UTe_2

Measurements of UTe_2 Fermi surfaces have reached broad agreement regarding the existence of two cylindrical, quasi-2D bands with a hole-type band around the **X** point and an electron-type band around the **Y** point of the Brillouin zone (*45, 49*). However, these quasi-2D Fermi surfaces are associated with U-*6d* and Te-*5p* orbitals, despite consensus that heavy *f*-electron correlations and the Kondo effect should play an important role in the low-temperature electronic structure. How this heavy electron physics impacts the Fermi surface is a matter of ongoing debate. We therefore first review the experimental results.

Angle-resolved photoemission spectroscopy (ARPES) reports of the Fermi surface support the existence of a heavy U band centered on either the Γ (*44*) or Z point (*45*) of the Brillouin zone. This band is found to be approximately spherical and, from gradient analysis of the intensity map, has a $\boldsymbol{k}$-space radius of ~0.2 $Å^{-1}$. Quantum oscillation experiments by Broyles *et al.* (*46*) found three low frequency, angle-independent peaks F_α, F_β, F_γ indicative of a spherical pocket with radius ~0.2 $Å^{-1}$. However, Weinberger *et al.* (*50*) observe only one low frequency peak (206 T) and notably this peak does not exhibit the same angular dependence as those observed in Ref. 46. Instead of a closed Fermi surface Weinberger *et al*. propose that *f*-electron hybridization induces significant warping of the quasi-2D Fermi surfaces along the k_z axis. The low frequency signal observed by Broyles *et al.* is then attributed to quantum interference effects between these hybridized bands (*50*).

Theoretical work has found that these interpretations of the Fermi surface are dependent on the degree of low-temperature hybridization. Calculations employing density functional theory (DFT) introduce an on-site Coulomb repulsion term U to describe *f*-electron correlations (*51*). Tuning this variable from 1 eV to 2 eV results in a Liftshitz transition of the Fermi surface at U ~ 1.6 eV. An intermediate value of U produces both the quasi-2D Fermi surface sheets and a pocket which encloses the Z point consistent with ARPES measurements. An intermediate value for U reflects more itinerant *f*-electrons expected for the Kondo effect at low temperature. Furthermore, both tight binding and DFT+DMFT (dynamical mean field theory) calculations of the Fermi surface reproduce this 3D Fermi surface component at low temperature and ambient pressure while also supporting B_{3u} symmetry of the triplet order parameter (*52*,*53*).

Theoretical calculations therefore indicate that Kondo hybridization at low temperature increases the 3D character of the Fermi surface. This 3D character may manifest as a simple warping of the quasi-2D sheets or, for stronger hybridization, the Fermi surface may be forced to enclose the Z point generating a truly 3D Fermi surface. In any case, the presence of a Fano peak in differential conductance measurements as well as *c*-axis transport measurements highlight the role of Kondo coherence at low temperatures and suggest that the low-temperature electronic structure of UTe_2 must take these hybridization effects into account (*26*,*54*). Whether this hybridization is enough to enforce the presence of a closed, 3D Fermi surface is unresolved. Future experiments, including further low frequency quantum oscillation measurements or STM quasiparticle interference imaging, should contribute further to determining the true Fermi surface of UTe_2.

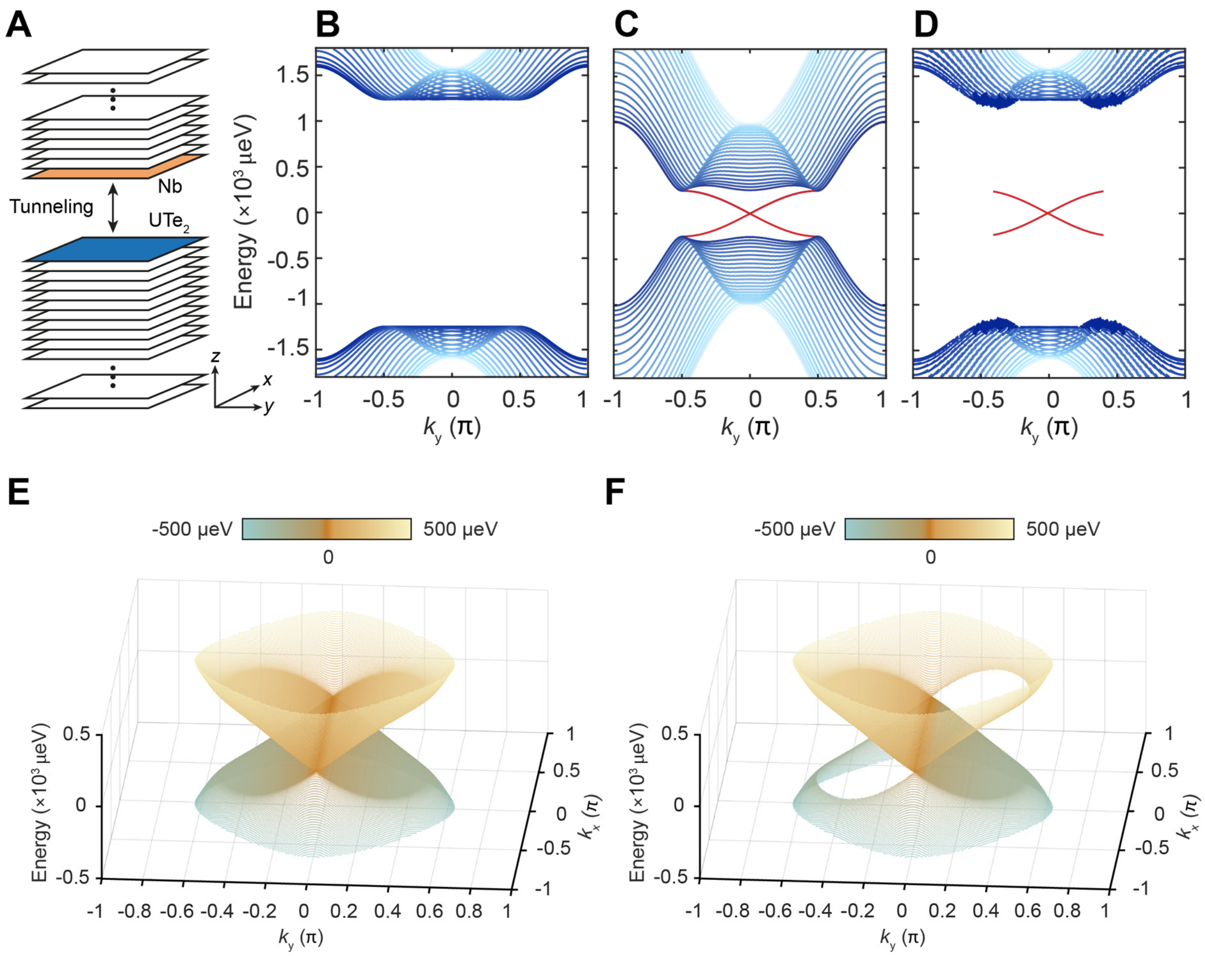

Fig. S1. Slab calculations of SIP model.

(**A**) Layered structure of SIP model stacked in the z direction, and continuous in x, y directions. (**B**) The surface band dispersion of Nb (indicated by the orange layer) when $M = 0$. In all the band dispersion calculations, the red dispersion lines denote the superconductive TSB. The shading of the blue dispersion lines highlight the low-energy band structure phenomena, and the excitations further from the Fermi level are less relevant to the tunneling process. (**C**) The surface band dispersion of UTe_2 (indicated by the blue layer) for non-chiral B_{3u} pairing when $M = 0$. The TSB is presented in red to distinguish these states from those of the bulk. (**D**) The surface band dispersion of Nb on the orange layer when $M = 0.2$ meV. Bulk states of UTe_2 within the energy of the Nb superconducting gap are forbidden to tunnel into Nb. Only the TSB of UTe_2 can tunnel into the Nb surface, which contributes to the tunneling current near zero energy. It can lead to sharp zero bias peak in differential conductance measurements between UTe_2 and Nb. In the calculation, we plot the bands whose wavefunction weight exceeds a certain lower bound (10^{-3} weight on the top surfaces of Nb and UTe_2, respectively). (**E**) 3D representation of the non-chiral TSB model used throughout. (**F**) 3D representation of the chiral TSB model used throughout.

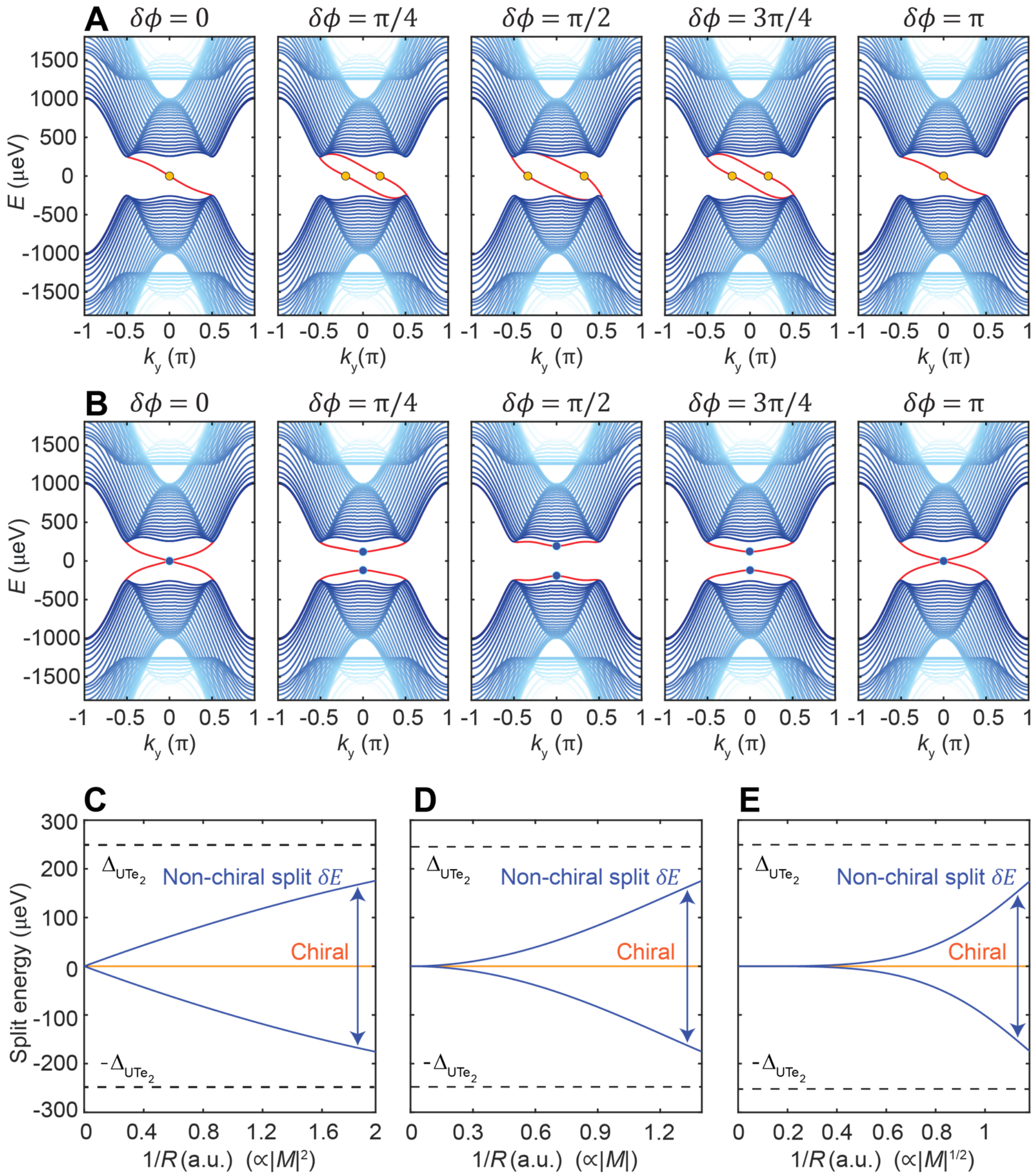

Fig. S2. Evolution of in-gap states vs. the relative phase $\delta\phi$ between Nb and UTe_2.
(**A**) Calculated quasiparticle bands within the SIP interface for chiral order parameter $A_u + iB_{3u}$. The chiral order parameter breaks time-reversal symmetry. The existence of its zero-energy states is therefore unaffected by tunneling to the *s*-wave Nb tip. (**B**) Calculated quasiparticle bands within the SIP interface for non-chiral order parameter B_{3u}. The tunneling matrix element $|M|$ is fixed while $\delta\phi$ evolves from 0 to π. The zero-energy states disappear due to broken time-reversal symmetry of the Nb-UTe_2 system at $\delta\phi = \pi/2$. (**C-E**) Energy splitting of zero-energy surface state derived from the model presented in Section 5. The relative phase $\delta\phi$ is kept fixed at π/2 while the tunneling matrix element $|M|$ is increased. We present three cases of split energy dependence on the tunneling matrix element $1/R \propto |M|^n$ with $n = 2, 1, 0.5$. $1/R \propto |M|$ in D is quantitively similar to the experimental data in Main Text Fig. 5D. Thus we choose to present D in Main Text Fig. 3D.

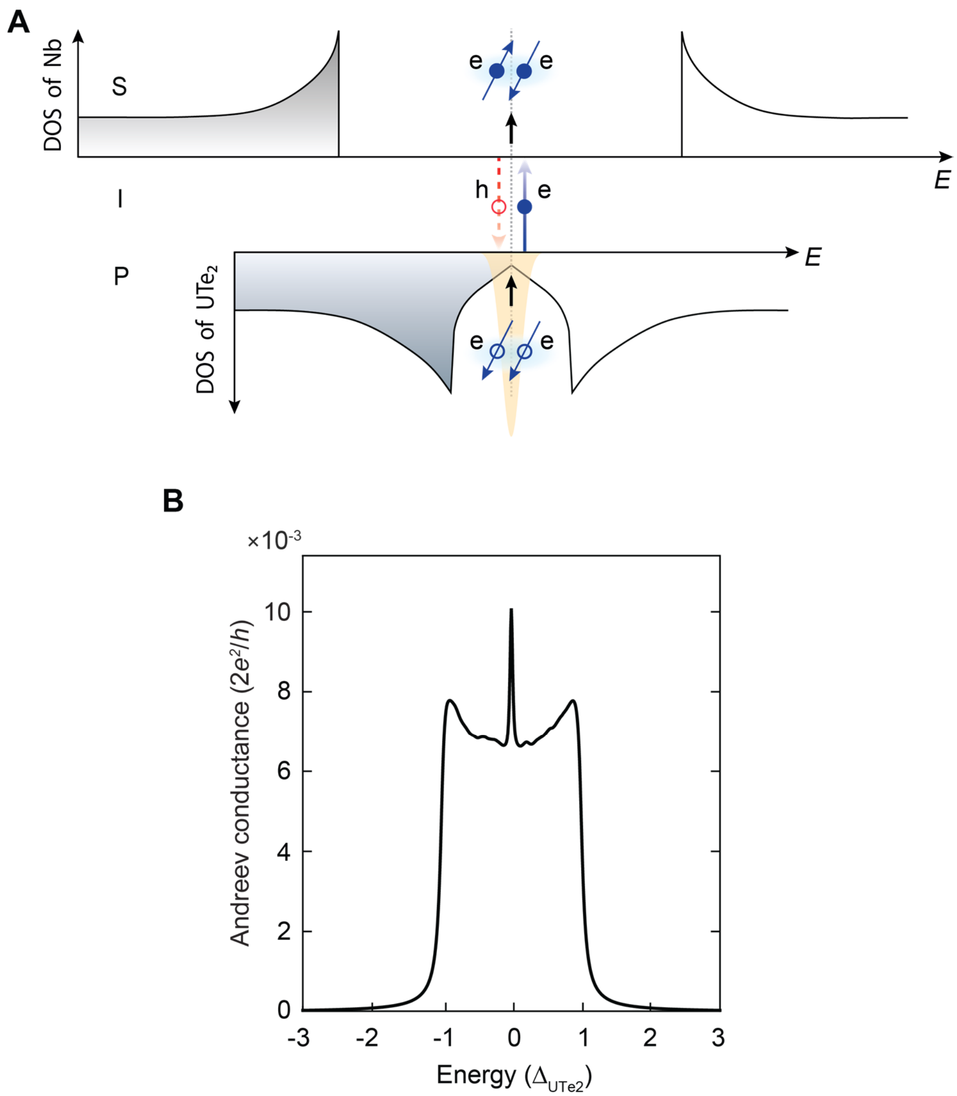

Fig. S3. TSB generated Andreev conductance in the SIP model.
(**A**) Schematic of the TSB generated Andreev tunneling to the *s*-wave electrode, through two quasiparticle transport process. (**B**) Calculated Andreev conductance $a(V)$ in the SIP model. Hence, the SIP model predicts a sharp peak in Andreev conductance surrounding zero-bias if the TSB is that of a *p*-wave, nodal, topological superconductor that mediates the *s*-wave to *p*-wave electronic transport processes. In this figure we have divided the total Andreev conductance by the number of transverse $k_{\parallel}$channels to mimic the point tunneling of STM.

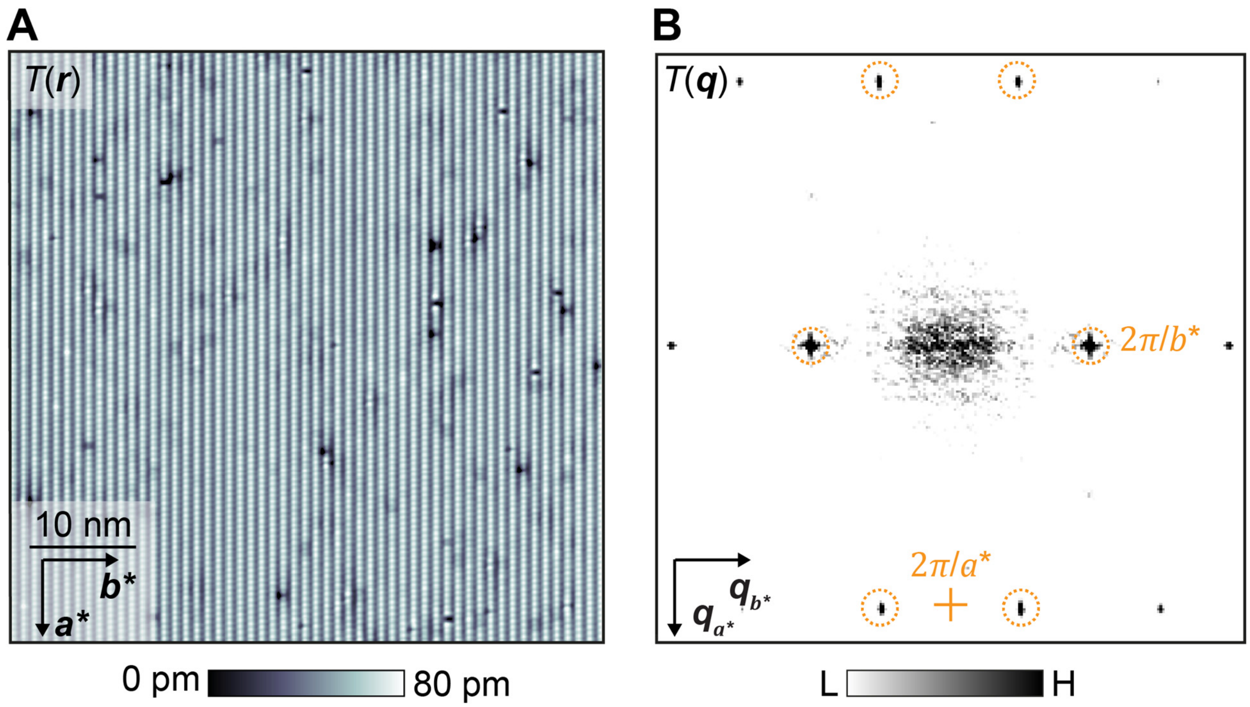

Fig. S4. Topographic image measured by using superconducting tip.
(A) Typical topographic image $T(\boldsymbol{r})$ of UTe_2 (0-11) surface measured with a superconducting STM tip. (**B**) Measured $T(\boldsymbol{q})$, the Fourier transform of $T(\boldsymbol{r})$, with the surface reciprocal-lattice points labelled as dashed circles.

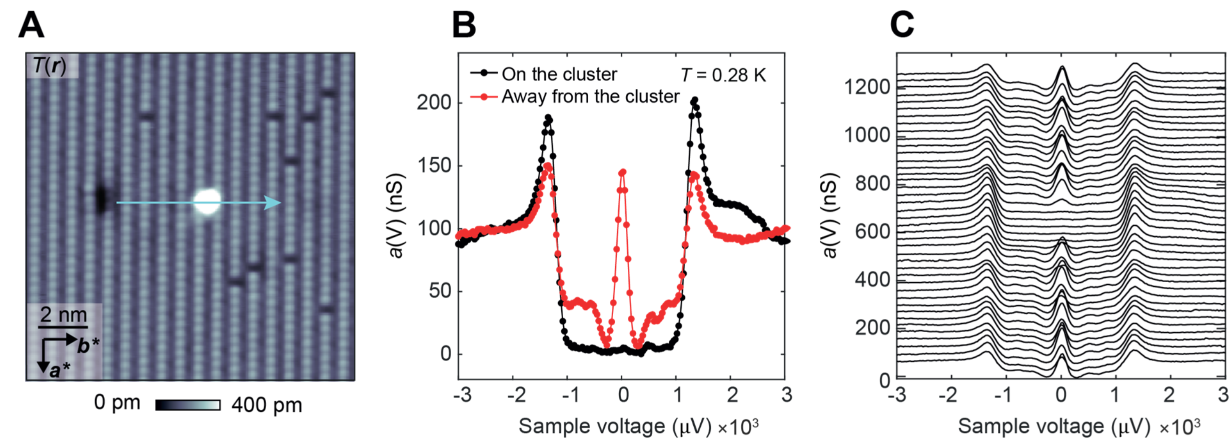

Fig. S5. Linecut over impurity adatom cluster.
(A) Topographic image of UTe_2 (0 –1 1) surface measured at $T = 280$ mK. The high intensity near the center is a cluster of impurity atoms. (**B**) Differential conductance spectra recorded away from (red) and upon (black) the adatom cluster. Observed sub-gap features across the cleave surface of the UTe_2 falls to zero on the adatom cluster. (**C**) Evolution of the Andreev conductance across the impurity cluster measured along the blue arrow indicated in A. The conductance of sub-gap features collapses to zero as the STM tip measures across the impurity cluster.

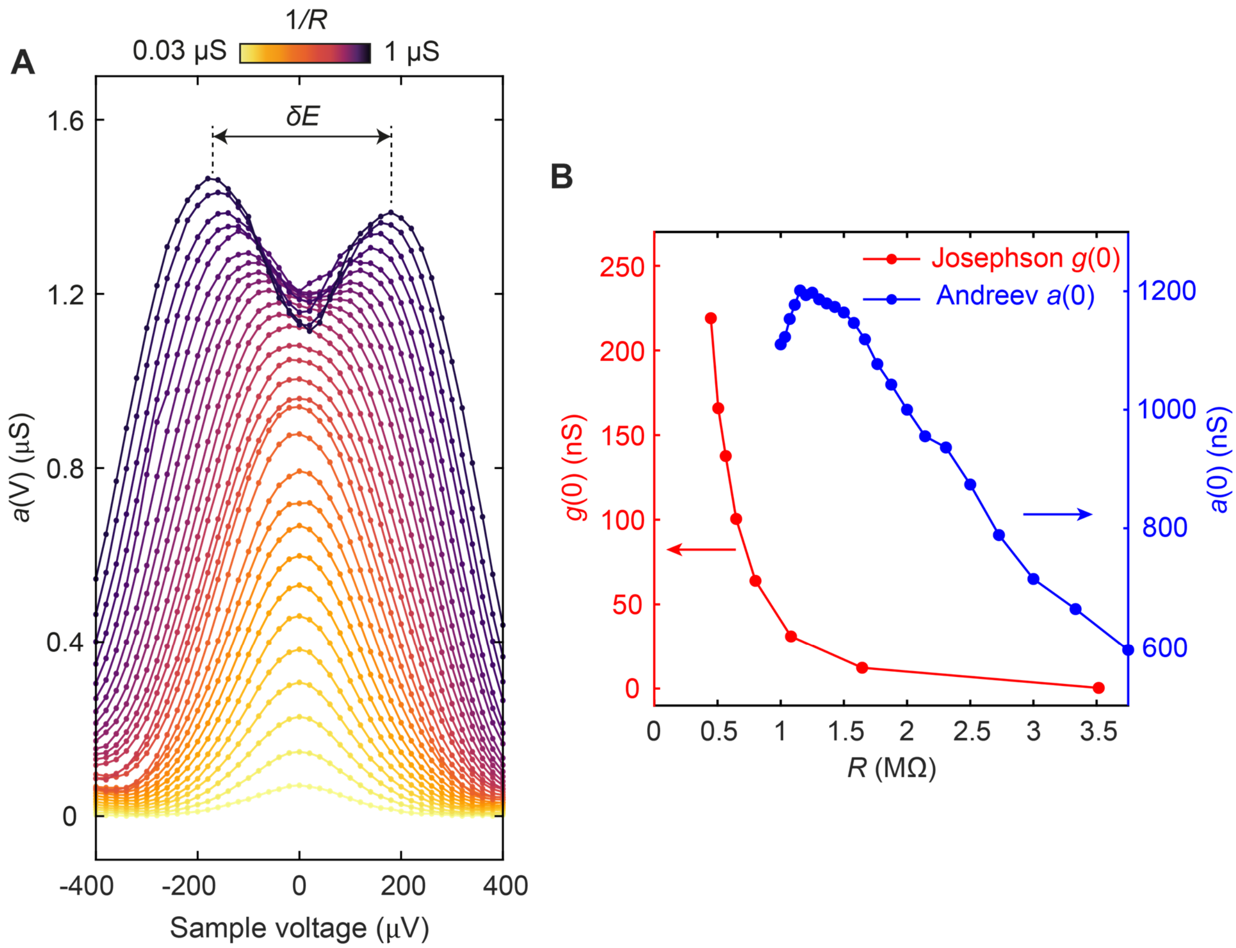

Fig. S6. Intensity and evolution of $dI/dV|_{\mathrm{SIP}}$ rules out Josephson currents.
(**A**) Measured evolution of differential Andreev conductance ($a(V) \equiv dI/dV|_{\mathrm{SIP}}$) spectra as a function of decreasing junction resistance R. (**B**) Comparison between the measured Andreev zero-bias conductance $a(0)$ of Nb/UTe_2 and Josephson zero-bias conductance $g(0)$ of Nb/$NbSe_2$ versus junction resistance R. The behaviour of the zero-bias conductance in the two effects are distinctly different and both the magnitude and R dependence of $a(0)$ are strongly inconsistent with what is expected in the case of Josephson tunneling between Nb and UTe_2.

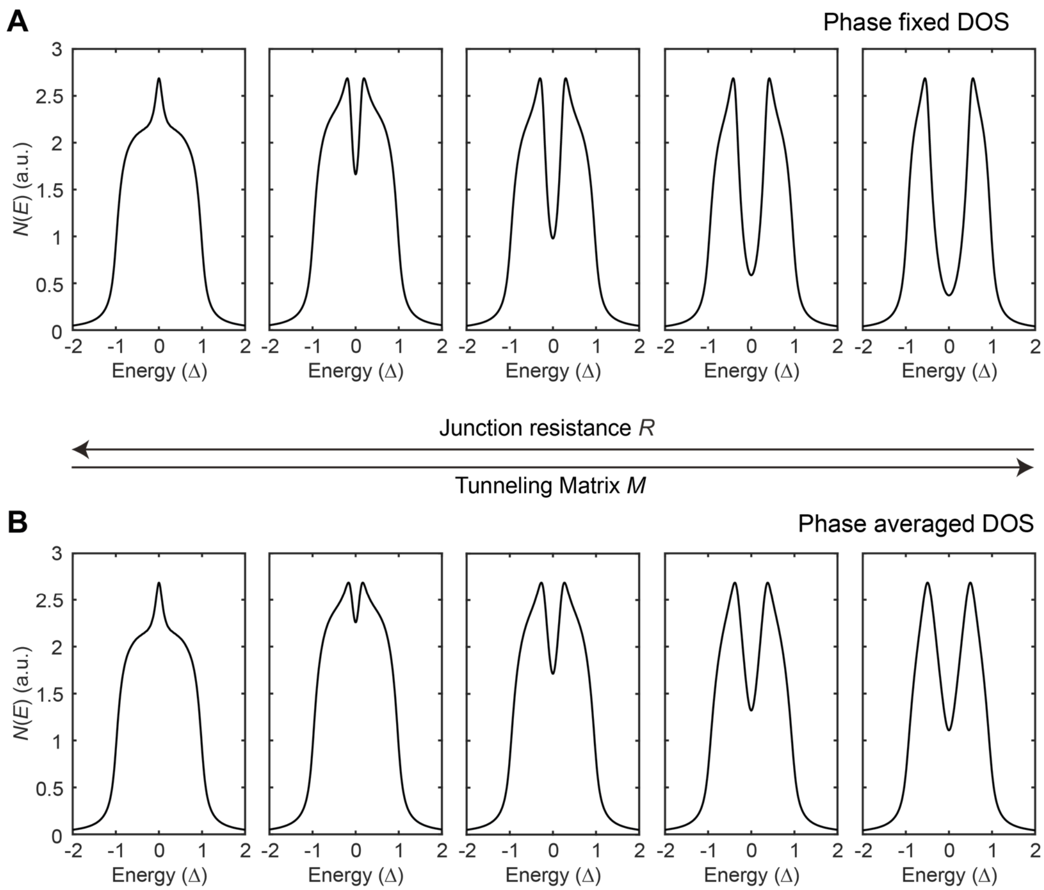

Fig. S7. Phase fluctuation effect on tip-induced time-reversal symmetry breaking.
(**A**) The calculated TSB density-of-states $N(E)$ when $\delta\phi = \frac{\pi}{2}$. (**B**) The calculated TSB density-of-states $N(E)$ when $\delta\phi$ is averaged with equal probability over the range $0 < \delta\phi < \pi$. The fact that the zero-bias peak splitting survives under these two extreme limits demonstrates that phase fluctuations will not destroy the signature of tip-induced time-reversal symmetry breaking in the SIP model.

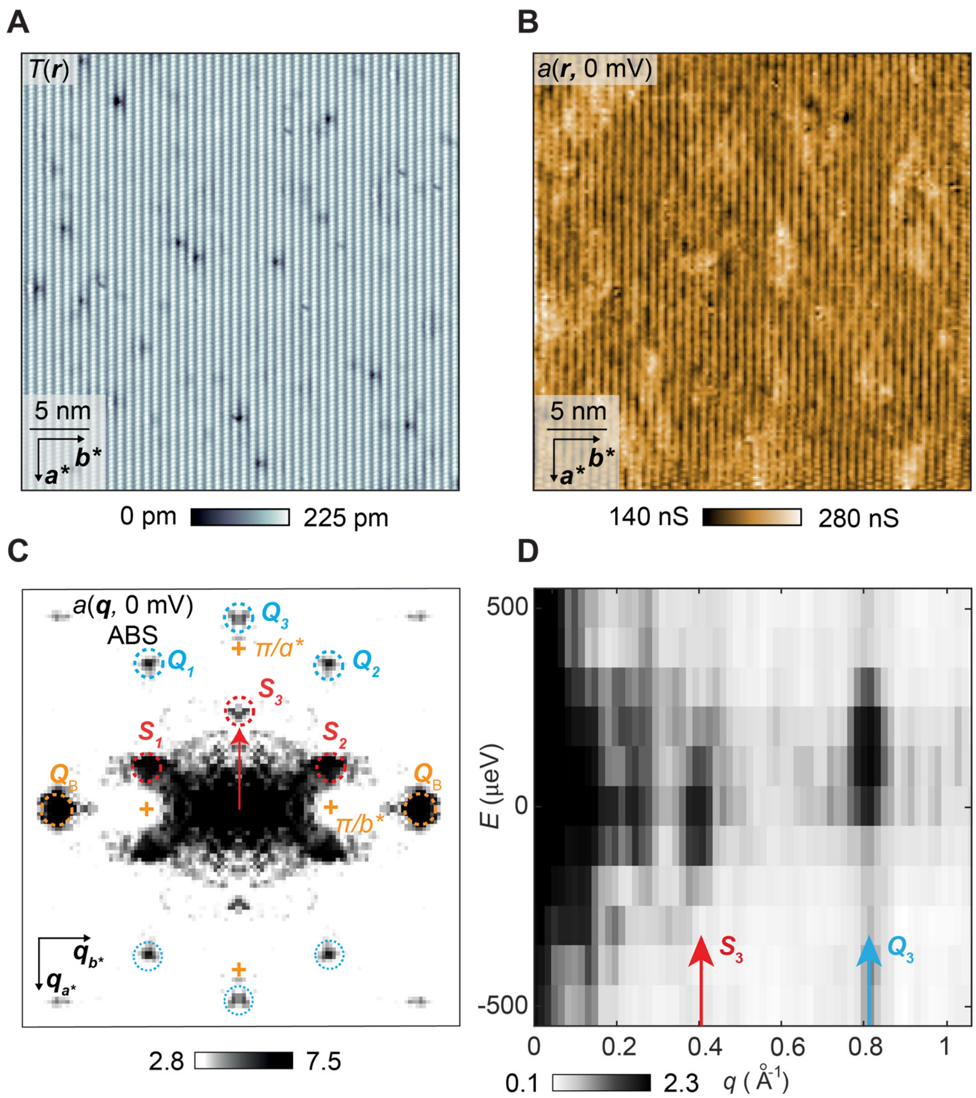

Fig. S8. S_3 not consistent with superconductivity induced CDW.

(**A**) Topograph of the (0 -1 1) cleave surface. (**B**) Andreev conductance $a(\boldsymbol{r}, 0\,\mathrm{mV})$ map demonstrating the real space modulation of the zero-energy peak. It is measured at the same FOV as in A. (**C**) Power spectral density Fourier transform of B. Reciprocal lattice points are indicated by orange circles, CDW modulations are indicated by blue circles, and the three new scattering wavevectors $\boldsymbol{S}_i$ ($i = 1,2,3$) are labelled by red circles. (**D**) Linecut from (0, 0) to (0, 1) $Å^{-1}$ in C. The putative internodal scattering $\boldsymbol{S}_3$ wavevector is indicated by a red arrow. The prevenient CDW modulation $\boldsymbol{Q}_3$ is indicated by a blue arrow.

References and Notes

1. M. R. Norman, The challenge of unconventional superconductivity. *Science* **332**, 196–200 (2011). doi:10.1126/science.1200181 Medline

2. P. W. Anderson, P. Morel, Generalized Bardeen-Cooper-Schrieffer states and the proposed low-temperature phase of liquid He^3. *Phys. Rev.* **123**, 1911–1934 (1961). doi:10.1103/PhysRev.123.1911

3. R. Balian, N. R. Werthamer, Superconductivity with pairs in a relative *p* wave. *Phys. Rev.* **131**, 1553–1564 (1963). doi:10.1103/PhysRev.131.1553

4. D. Vollhardt, P. Woelfle, *The Superfluid Phases of Helium 3* (Taylor & Francis, 1990).

5. A. J. Leggett, *Quantum Liquids: Bose Condensation and Cooper Pairing in Condensed-Matter Systems* (Oxford Univ. Press, 2006).

6. A. P. Schnyder, S. Ryu, A. Furusaki, A. W. W. Ludwig, Classification of topological insulators and superconductors in three spatial dimensions. *Phys. Rev. B* **78**, 195125 (2008). doi:10.1103/PhysRevB.78.195125

7. A. P. Schnyder, P. M. R. Brydon, Topological surface states in nodal superconductors. *J. Phys. Condens. Matter* **27**, 243201 (2015). doi:10.1088/0953-8984/27/24/243201 Medline

8. C. Kallin, J. Berlinsky, Chiral superconductors. *Rep. Prog. Phys.* **79**, 054502 (2016). doi:10.1088/0034-4885/79/5/054502 Medline

9. Supplementary materials.

10. D. Aoki, A. Nakamura, F. Honda, D. Li, Y. Homma, Y. Shimizu, Y. J. Sato, G. Knebel, J.-P. Brison, A. Pourret, D. Braithwaite, G. Lapertot, Q. Niu, M. Vališka, H. Harima, J. Flouquet, Unconventional superconductivity in heavy fermion UTe_2. *J. Phys. Soc. Jpn.* **88**, 043702 (2019). doi:10.7566/JPSJ.88.043702

11. S. Ran, C. Eckberg, Q.-P. Ding, Y. Furukawa, T. Metz, S. R. Saha, I.-L. Liu, M. Zic, H. Kim, J. Paglione, N. P. Butch, Nearly ferromagnetic spin-triplet superconductivity. *Science* **365**, 684–687 (2019). doi:10.1126/science.aav8645 Medline

12. D. Aoki, J.-P. Brison, J. Flouquet, K. Ishida, G. Knebel, Y. Tokunaga, Y. Yanase, Unconventional superconductivity in UTe_2. *J. Phys. Condens. Matter* **34**, 243002 (2022). doi:10.1088/1361-648X/ac5863 Medline

13. P. F. S. Rosa, A. Weiland, S. S. Fender, B. L. Scott, F. Ronning, J. D. Thompson, E. D. Bauer, S. M. Thomas, Single thermodynamic transition at 2 K in superconducting UTe_2 single crystals. *Commun. Mater.* **3**, 33 (2022). doi:10.1038/s43246-022-00254-2

14. Y. Tokunaga, H. Sakai, S. Kambe, T. Hattori, N. Higa, G. Nakamine, S. Kitagawa, K. Ishida, A. Nakamura, Y. Shimizu, Y. Homma, D. Li, F. Honda, D. Aoki, ^{125}Te-NMR study on a single crystal of heavy fermion superconductor UTe_2. *J. Phys. Soc. Jpn.* **88**, 073701 (2019). doi:10.7566/JPSJ.88.073701

15. G. Nakamine, S. Kitagawa, K. Ishida, Y. Tokunaga, H. Sakai, S. Kambe, A. Nakamura, Y. Shimizu, Y. Homma, D. Li, F. Honda, D. Aoki, Superconducting properties of heavy

fermion UTe_2 revealed by ^{125}Te-nuclear magnetic resonance. *J. Phys. Soc. Jpn.* **88**, 113703 (2019). doi:10.7566/JPSJ.88.113703

16. H. Sakai, P. Opletal, Y. Tokiwa, E. Yamamoto, Y. Tokunaga, S. Kambe, Y. Haga, Single crystal growth of superconducting UTe_2 by molten salt flux method. *Phys. Rev. Mater.* **6**, 073401 (2022). doi:10.1103/PhysRevMaterials.6.073401
17. H. Matsumara, H. Fujibayashi, K. Kinjo, S. Kitagawa, K. Ishida, Y. Tokunaga, H. Sakai, S. Kambe, A. Nakamura, Y. Shimizu, Y. Homma, D. Li, F. Honda, D. Aoki, Large reduction in the *a*-axis Knight shift on UTe_2 with $T_c = 2.1$ K. *J. Phys. Soc. Jpn.* **92**, 063701 (2023). doi:10.7566/JPSJ.92.063701
18. H. Fujibayashi, G. Nakamine, K. Kinjo, S. Kitagawa, K. Ishida, Y. Tokunaga, H. Sakai, S. Kambe, A. Nakamura, Y. Shimizu, Y. Homma, D. Li, F. Honda, D. Aoki, Superconducting order parameter in UTe_2 determined by Knight shift measurement. *J. Phys. Soc. Jpn.* **91**, 043705 (2022). doi:10.7566/JPSJ.91.043705
19. T. Metz, S. Bae, S. Ran, I.-L. Liu, Y. S. Eo, W. T. Fuhrman, D. F. Agterberg, S. M. Anlage, N. P. Butch, J. Paglione, Point-node gap structure of the spin-triplet superconductor UTe_2. *Phys. Rev. B* **100**, 220504(R) (2019). doi:10.1103/PhysRevB.100.220504 Medline
20. S. Suetsugu, M. Shimomura, M. Kamimura, T. Asaba, H. Asaeda, Y. Kosuge, Y. Sekino, S. Ikemori, Y. Kasahara, Y. Kohsaka, M. Lee, Y. Yanase, H. Sakai, P. Opletal, Y. Tokiwa, Y. Haga, Y. Matsuda, Fully gapped pairing state in spin-triplet superconductor UTe_2. *Sci. Adv.* **10**, eadk3772 (2024). doi:10.1126/sciadv.adk3772 Medline
21. S. Kittaka, Y. Shimizu, T. Sakakibara, A. Nakamura, D. Li, Y. Homma, F. Honda, D. Aoki, K. Machida, Orientation of point nodes and nonunitary triplet pairing tuned by the easy-axis magnetization in UTe2. *Phys. Rev. Res.* **2**, 032014(R) (2020). doi:10.1103/PhysRevResearch.2.032014
22. I. M. Hayes, D. S. Wei, T. Metz, J. Zhang, Y. S. Eo, S. Ran, S. R. Saha, J. Collini, N. P. Butch, D. F. Agterberg, A. Kapitulnik, J. Paglione, Multicomponent superconducting order parameter in UTe_2. *Science* **373**, 797–801 (2021). doi:10.1126/science.abb0272 Medline
23. L. P. Cairns, C. R. Stevens, C. D. O'Neill, A. Huxley, Composition dependence of the superconducting properties of UTe_2. *J. Phys. Condens. Matter* **32**, 415602 (2020). doi:10.1088/1361-648X/ab9c5d Medline
24. Y. Iguchi, H. Man, S. M. Thomas, F. Ronning, P. F. S. Rosa, K. A. Moler, Microscopic imaging homogeneous and single phase superfluid density in UTe_2. *Phys. Rev. Lett.* **130**, 196003 (2023). doi:10.1103/PhysRevLett.130.196003 Medline
25. K. Ishihara, M. Roppongi, M. Kobayashi, K. Imamura, Y. Mizukami, H. Sakai, P. Opletal, Y. Tokiwa, Y. Haga, K. Hashimoto, T. Shibauchi, Chiral superconductivity in UTe_2 probed by anisotropic low-energy excitations. *Nat. Commun.* **14**, 2966 (2023). doi:10.1038/s41467-023-38688-y Medline
26. L. Jiao, S. Howard, S. Ran, Z. Wang, J. O. Rodriguez, M. Sigrist, Z. Wang, N. P. Butch, V. Madhavan, Chiral superconductivity in heavy-fermion metal UTe_2. *Nature* **579**, 523–527 (2020). doi:10.1038/s41586-020-2122-2 Medline

27. M. O. Ajeesh, M. Bordelon, C. Girod, S. Mishra, F. Ronning, E. D. Bauer, B. Maiorov, J. D. Thompson, P. F. S. Rosa, S. M. Thomas, The fate of time-reversal symmetry breaking in UTe_2. *Phys. Rev. X* **13**, 041019 (2023). doi:10.1103/PhysRevX.13.041019

28. J. E. Hoffman, K. McElroy, D.-H. Lee, K. M. Lang, H. Eisaki, S. Uchida, J. C. Davis, Imaging quasiparticle interference in $Bi_2Sr_2CaCu_2O_{8+\delta}$. *Science* **297**, 1148–1151 (2002). doi:10.1126/science.1072640 Medline

29. T. Hanaguri, Y. Kohsaka, J. C. Davis, C. Lupien, I. Yamada, M. Azuma, M. Takano, K. Ohishi, H. Takagi, Low-energy spectroscopic mapping studies in optimally-doped $Ca_{2-x}Na_xCuO_2Cl_2$. *Physica C* **460**, 954–955 (2007). doi:10.1016/j.physc.2007.03.324

30. M. P. Allan, F. Massee, D. K. Morr, J. Van Dyke, A. W. Rost, A. P. Mackenzie, C. Petrovic, J. C. Davis, Imaging Cooper pairing of heavy fermions in $CeCoIn_5$. *Nat. Phys.* **9**, 468–473 (2013). doi:10.1038/nphys2671

31. M. P. Allan, A. W. Rost, A. P. Mackenzie, Y. Xie, J. C. Davis, K. Kihou, C. H. Lee, A. Iyo, H. Eisaki, T.-M. Chuang, Anisotropic energy gaps of iron-based superconductivity from intraband quasiparticle interference in LiFeAs. *Science* **336**, 563–567 (2012). doi:10.1126/science.1218726 Medline

32. P. O. Sprau, A. Kostin, A. Kreisel, A. E. Böhmer, V. Taufour, P. C. Canfield, S. Mukherjee, P. J. Hirschfeld, B. M. Andersen, J. C. S. Davis, Discovery of orbital-selective Cooper pairing in FeSe. *Science* **357**, 75–80 (2017). doi:10.1126/science.aal1575 Medline

33. R. Sharma, S. D. Edkins, Z. Wang, A. Kostin, C. Sow, Y. Maeno, A. P. Mackenzie, J. C. S. Davis, V. Madhavan, Momentum-resolved superconducting energy gaps of Sr_2RuO_4 from quasiparticle interference imaging. *Proc. Natl. Acad. Sci. U.S.A.* **117**, 5222–5227 (2020). doi:10.1073/pnas.1916463117 Medline

34. Q. Gu, J. P. Carroll, S. Wang, S. Ran, C. Broyles, H. Siddiquee, N. P. Butch, S. R. Saha, J. Paglione, J. C. S. Davis, X. Liu, Detection of a pair density wave state in UTe_2. *Nature* **618**, 921–927 (2023). doi:10.1038/s41586-023-05919-7 Medline

35. A. Aishwarya, J. May-Mann, A. Raghavan, L. Nie, M. Romanelli, S. Ran, S. R. Saha, J. Paglione, N. P. Butch, E. Fradkin, V. Madhavan, Magnetic-field-sensitive charge density waves in the superconductor UTe_2. *Nature* **618**, 928–933 (2023). doi:10.1038/s41586-023-06005-8 Medline

36. S. Bae, H. Kim, Y. S. Eo, S. Ran, I.-L. Liu, W. T. Fuhrman, J. Paglione, N. P. Butch, S. M. Anlage, Anomalous normal fluid response in a chiral superconductor UTe_2. *Nat. Commun.* **12**, 2644 (2021). doi:10.1038/s41467-021-22906-6 Medline

37. Q. H. Wang, D. H. Lee, Quasiparticle scattering interference in high-temperature superconductors. *Phys. Rev. B* **67**, 020511(R) (2003). doi:10.1103/PhysRevB.67.020511

38. M. H. Hamidian, S. D. Edkins, S. H. Joo, A. Kostin, H. Eisaki, S. Uchida, M. J. Lawler, E.-A. Kim, A. P. Mackenzie, K. Fujita, J. Lee, J. C. Davis, Detection of a Cooper-pair density wave in $Bi_2Sr_2CaCu_2O_{8+x}$. *Nature* **532**, 343–347 (2016). doi:10.1038/nature17411 Medline

39. D. Cho, K. M. Bastiaans, D. Chatzopoulos, G. D. Gu, M. P. Allan, A strongly inhomogeneous superfluid in an iron-based superconductor. *Nature* **571**, 541–545 (2019). doi:10.1038/s41586-019-1408-8 Medline

40. X. Liu, Y. X. Chong, R. Sharma, J. C. Davis, Discovery of a Cooper-pair density wave state in a transition-metal dichalcogenide. *Science* **372**, 1447–1452 (2021). doi:10.1126/science.abd4607

41. X. Liu, Y. X. Chong, R. Sharma, J. C. S. Davis, Atomic-scale visualization of electronic fluid flow. *Nat. Mater.* **20**, 1480–1484 (2021). doi:10.1038/s41563-021-01077-1 Medline

42. S. M. O'Mahony, W. Ren, W. Chen, Y. X. Chong, X. Liu, H. Eisaki, S. Uchida, M. H. Hamidian, J. C. S. Davis, On the electron pairing mechanism of copper-oxide high temperature superconductivity. *Proc. Natl. Acad. Sci. U.S.A.* **119**, e2207449119 (2022). doi:10.1073/pnas.2207449119 Medline

43. W. Chen, W. Ren, N. Kennedy, M. H. Hamidian, S. Uchida, H. Eisaki, P. D. Johnson, S. M. O'Mahony, J. C. S. Davis, Identification of a nematic pair density wave state in $Bi_2Sr_2CaCu_2O_{8+x}$. *Proc. Natl. Acad. Sci. U.S.A.* **119**, e2206481119 (2022). doi:10.1073/pnas.2206481119 Medline

44. S. Fujimori, I. Kawasaki, Y. Takeda, H. Yamagami, A. Nakamura, Y. Homma, D. Aoki, Electronic structure of UTe_2 studied by photoelectron spectroscopy. *J. Phys. Soc. Jpn.* **88**, 103701 (2019). doi:10.7566/JPSJ.88.103701

45. L. Miao, S. Liu, Y. Xu, E. C. Kotta, C.-J. Kang, S. Ran, J. Paglione, G. Kotliar, N. P. Butch, J. D. Denlinger, L. A. Wray, Low energy band structure and symmetries of UTe_2 from angle-resolved photoemission spectroscopy. *Phys. Rev. Lett.* **124**, 076401 (2020). doi:10.1103/PhysRevLett.124.076401 Medline

46. C. Broyles, Z. Rehfuss, H. Siddiquee, J. A. Zhu, K. Zheng, M. Nikolo, D. Graf, J. Singleton, S. Ran, Revealing a 3D Fermi surface pocket and electron-hole tunneling in UTe_2 with quantum oscillations. *Phys. Rev. Lett.* **131**, 036501 (2023). doi:10.1103/PhysRevLett.131.036501 Medline

47. Q. Gu, S. Wang, J. P. Carroll, K. Zhussupbekov, C. Broyles, S. Ran, N. P. Butch, S. Saha, J. Paglione, X. Liu, J. C. S. Davis, D.-H. Lee, Pair Wave Function Symmetry in UTe_2 from Zero-Energy Surface State Visualization [Data set], version 2, Zenodo (2025); https://doi.org/10.5281/zenodo.15021425.

48. D. Agterberg, J. C. Davis, S. D. Edkins, E. Fradkin, D. J. Van Harlingen, S. A. Kivelson, P. A. Lee, L. Radzihovsky, J. M. Tranquada, Y. Wang, The physics of pair-density waves: Cuprate superconductors and beyond. *Annu. Rev. Condens. Matter Phys.* **11**, 231–270 (2020). doi:10.1146/annurev-conmatphys-031119-050711

49. D. Aoki, H. Sakai, P. Opletal, Y. Tokiwa, J. Ishizuka, Y. Yanase, H. Harima, A. Nakamura, D. Li, Y. Homma, Y. Shimizu, G. Knebel, J. Flouquet, Y. Haga, First observation of the de Haas–van Alphen effect and Fermi surfaces in the unconventional superconductor UTe_2. *J. Phys. Soc. Jpn.* **91**, 083704 (2022). doi:10.7566/JPSJ.91.083704

50. T. I. Weinberger, Z. Wu, D. E. Graf, Y. Skourski, A. Cabala, J. Pospíšil, J. Prokleška, T. Haidamak, G. Bastien, V. Sechovský, G. G. Lonzarich, M. Vališka, F. M. Grosche, A. G.

Eaton, Quantum interference between quasi-2D Fermi surface sheets in UTe_2. *Phys. Rev. Lett.* **132**, 266503 (2024). doi:10.1103/PhysRevLett.132.266503 Medline

51. J. Ishizuka, S. Sumita, A. Daido, Y. Yanase, Insulator-metal transition and topological superconductivity in UTe_2 from a first-principles calculation. *Phys. Rev. Lett.* **123**, 217001 (2019). doi:10.1103/PhysRevLett.123.217001 Medline

52. J. Ishizuka, Y. Yanase, Periodic Anderson model for magnetism and superconductivity in UTe_2. *Phys. Rev. B* **103**, 094504 (2021). doi:10.1103/PhysRevB.103.094504

53. H. Choi, S. Lee, B. Yang, Correlated normal state fermiology and topological superconductivity in UTe_2. *Commun. Phys.* **7**, 273 (2024). doi:10.1038/s42005-024-01708-4

54. Y. Eo, S. Liu, S. R. Saha, H. Kim, S. Ran, J. A. Horn, H. Hodovanets, J. Collini, T. Metz, W. T. Fuhrman, A. H. Nevidomskyy, J. D. Denlinger, N. P. Butch, M. S. Fuhrer, L. A. Wray, J. Paglione, *c*-axis transport in UTe_2: Evidence of three-dimensional conductivity component. *Phys. Rev. B* **106**, L060505 (2022). doi:10.1103/PhysRevB.106.L060505